Dynamic coupling and spin-wave dispersions in a magnetic hybrid system made of an artificial spin-ice structure and an extended NiFe underlayer (F)

R. Negrello, (iD) F. Montoncello, (iD) M. T. Kaffash, et al.

COLLECTIONS

Note: This paper is part of the Special Topic on Science and Technology of 3D Magnetic Nanostructures.

(F) This paper was selected as Featured
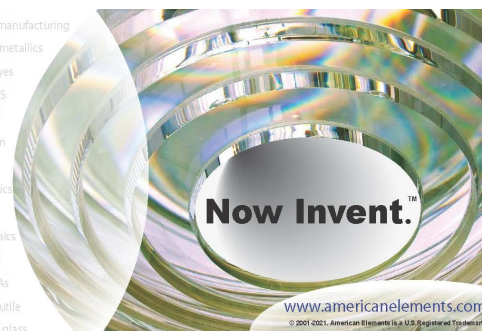
View Online   Export Citation   CrossMark

Dynamic coupling and spin-wave dispersions in a magnetic hybrid system made of an artificial spin-ice structure and an extended NiFe underlayer 🔵F

R. Negrello,[1] F. Montoncello,[1] 🔵 M. T. Kaffash,[2] 🔵 M. B. Jungfleisch,[2,a)] 🔵 and G. Gubbiotti[3] 🔵

AFFILIATIONS

[1] Dipartimento di Fisica e Scienze della Terra, Università di Ferrara, Ferrara, Italy
[2] Department of Physics and Astronomy, University of Delaware, Newark, Delaware 19716, USA
[3] Istituto Officina dei Materiali del Consiglio Nazionale delle Ricerche (IOM-CNR), c/o Dipartimento di Fisica e Geologia, Perugia I 06123, Italy

Note: This paper is part of the Special Topic on Science and Technology of 3D Magnetic Nanostructures.
a)Author to whom correspondence should be addressed: mbj@udel.edu

ABSTRACT

We present a combined experimental and numerical study of the spin-wave dispersion in a NiFe artificial spin-ice (ASI) system consisting of an array of stadium-shaped nanoislands deposited on the top of a continuous NiFe film with non-magnetic spacer layers of varying thickness. The spin-wave dispersion, measured by wavevector resolved Brillouin light scattering spectroscopy in the Damon–Eshbach configuration, consists of a rich number of modes, with either stationary or propagating character. We find that the lowest frequency mode displays a bandwidth of ~0.5 GHz, which is independent of the presence of the film underneath. On the contrary, the Brillouin light scattering intensity of some of the detected modes strongly depends on the presence of the extended thin-film underlayer. Micromagnetic simulations unveil the details of the dynamic coupling between the ASI lattice and film underlayer. Interestingly, the ASI lattice facilitates dynamics of the film either specific wavelengths or intensity modulation peculiar to the modes of the ASI elements imprinted in the film. Our results demonstrate that propagating spin waves can be modulated at the nanometer length scale by harnessing the dynamic mode coupling in the vertical, i.e., the out-of-plane direction of suitably designed magnonic structures.

I. INTRODUCTION

The strong coupling between nanoscale magnetic elements in two-dimensional arrays known as artificial spin ice (ASI) leads to frustrated magnetic states and results in highly degenerate energy landscapes.[1] These degenerate energy landscapes and the associated magnetic ordering in the lattice[2–13] enable the realization of reconfigurable magnonic crystals and devices. Various approaches have been proposed to utilize reconfigurability for an on-demand manipulation of the spin-wave (SW) propagation characteristics, dispersion,[14–17] and hybridizations.[18–20] To this end, Bhat et al. demonstrated spatially localized SW modes in a connected Kagome

lattice by microfocused Brillouin light scattering (BLS),[21] while Taghipour Kaffash et al. revealed SW channels in a honeycomb array of nanodisks using microfocused BLS.[22] Despite this progress in understanding the dynamics in ASI on the micro- and nanoscale using BLS imaging, the SW dispersion in these structures is much less explored experimentally[11,12,23] and theoretically.[3,24] Li et al. investigated the field-dependent spin-wave spectra of a square ASI using wavevector-resolved BLS and revealed the soft-mode behavior in the lattice while no sizable frequency dependence on the wavevector was found. Mamica et al.[11] studied the formation of magnon band structures and gaps in anti-spin-ice systems and found, by rotating the applied field direction, a transformation

of non-propagating modes into propagating SWs with a number of hybridizations. Iacocca and Heinonen[24] theoretically explored the influence of interfacial Dzyaloshinskii–Moriya interaction and the internal magnetization configuration within an ASI vertex on the magnon dispersion.

Furthermore, ASI structures are useful for the emerging field of *vertical magnonics* that explores alternative mechanisms for controlling SWs at the nanoscale,[25–27] and the concept of ASI is already extending into three dimensions.[28–33] A recent theoretical proposal to modify SW channels in an ASI system is based on an ASI/magnetic thin film underlayer system;[34] while not directly demonstrated, the results suggest the existence of a dispersive propagating mode in the ASI-based system. However, direct proof and experimental confirmation for such a dispersive magnon characteristic in these structures remained elusive until now.

Here, we couple a square ASI structure made of permalloy (NiFe) stadium-shaped nanoelements ("islands," in the following) to a continuous NiFe film underlayer to explore how the presence of the ASI affects the spin-wave properties in a film underlayer. We use a relatively strong magnetic field of 200 mT to ensure that the magnetic moments in a subset of islands are oriented almost parallel to the film magnetization, while the other subset is oriented in an onion-like state. Dependent on the separation between the underlayer and the ASI nanostructure, we observe rich SW spectra exhibiting characteristic mode dispersion crossings indicative of the dynamic coupling between the film Damon–Eshbach (DE) mode and the ASI modes. Furthermore, we find a dispersive magnon mode both in the isolated ASI without underlayer and in the hybrid structures. The experimental wavevector-resolved BLS spectroscopy measurements are interpreted through micromagnetic simulations, which reveal the BLS-active mode profiles, and link them to the behavior of the effective magnetic field. The existence and the significance of the dynamic coupling between the layers are also discussed as a function of the frequency and profile symmetry of the modes.

II. EXPERIMENTAL APPROACH AND MICROMAGNETIC FRAMEWORK

A. Sample fabrication and characterization

We use a multi-step lithography process for sample fabrication, which is discussed in detail in the supplementary material. The samples consist of (a) continuous $Ni_{81}Fe_{19}$ film (15 nm) (sample no. 1), (b) square ASI made of 15 nm thick $Ni_{81}Fe_{19}$ (sample no. 2), (c) $Ni_{81}Fe_{19}$ (15 nm) film with a 2 nm natural oxide spacer layer with a square ASI made of 15 nm thick $Ni_{81}Fe_{19}$ (sample no. 3), and (d) $Ni_{81}Fe_{19}$ (15 nm)/Al_2O_3 (10 nm) with a square ASI made of 15 nm thick $Ni_{81}Fe_{19}$ (sample no. 4). The nominal lattice constant is hence $a = 350$ nm, determining the Brillouin zone (BZ) boundary at $k = \pi/a = 0.9 \times 10^7$ rad/m. A representative scanning electron microscopy (SEM) image is shown in Fig. 1 (here shown sample no. 2). As shown in Fig. 1, we achieved excellent dimension control, size, and shape homogeneity over a large patterned area.

SW frequencies of the investigated samples have been measured by BLS spectroscopy from thermally excited SWs.[35,36] An external magnetic field $\mu_0 H = 200$ mT is applied along the y-direction (see Fig. 1) and perpendicular to the incidence plane, i.e., the
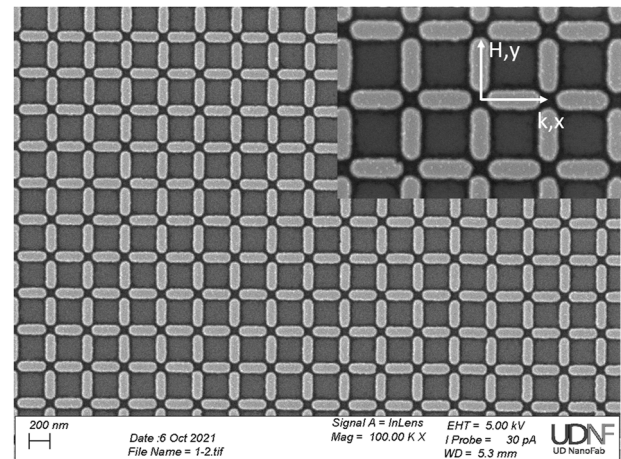

FIG. 1. SEM image of the artificial spin ice structure (sample no. 2). Arrows indicate the system of coordinate axes together with the direction of the applied magnetic field (H) and the probed SW wavevector (k).

wavevector is in the DE configuration. Due to the conservation of the in-plane momentum, we can detect the spin-wave wavevector by selecting the proper incidence angle of light with respect to the sample surface.[35,36] The magnitude of k is varied from $k = 0.08$ to 2.2×10^7 rad/m.

Figure 2 represents a sequence of the anti-Stokes side of the measured BLS spectra at the minimum wavevector. For sample no. 1 [Fig. 2(a)], only one peak is observed in the spectrum, corresponding to the film DE mode. For sample no. 2 [Fig. 2(b)], two major peaks (1) and (2) and a minor one (3) are observed. While the width of peak (2) seems to be independent of the sample, peak (1) is broader in coupled sample nos. 3 and 4, with the presence of an additional peak, labeled (5), visible as a left shoulder. Moreover, in the coupled samples, an additional peak (4) appears, slightly above peak (3) and with comparable intensity.

B. Micromagnetic framework and simulations

Micromagnetic simulations were performed using the graphic processing unit (GPU) accelerated software mumax³.[37] The system was designed as a 15 nm-thick layer onto a 15 nm-thick primitive cell of the ASI lattice and discretized in $4.0625 \times 4.0625 \times 5$ nm³ micromagnetic cells. The primitive cell is a 88×88 square (i.e., 357.5×357.5 nm²) in which two islands are included, represented as ellipses,[38] each made by 64×24 cells, i.e., 260×97.5 nm². Periodic boundary conditions are used in mumax³ in order to simulate an ideal, infinite system. The used magnetic parameters are saturation magnetization $M_s = 800$ kA/m, exchange stiffness $A = 13$ pJ/m, and gyromagnetic ratio $\gamma = 185$ rad GHz/T. A magnetic field $\mu_0 H = 200$ mT is applied perpendicularly to the direction x of the wavevector with a slight tilt angle of 1° to mimic realistic conditions. After relaxing the system from uniform saturation in the y-direction into the equilibrium magnetic configuration, we apply a uniform sinc pulse perpendicular to the plane to excite the system, collect the excited out-of-plane magnetization, and perform the time-space fast Fourier transform (FFT) to get either mode profiles
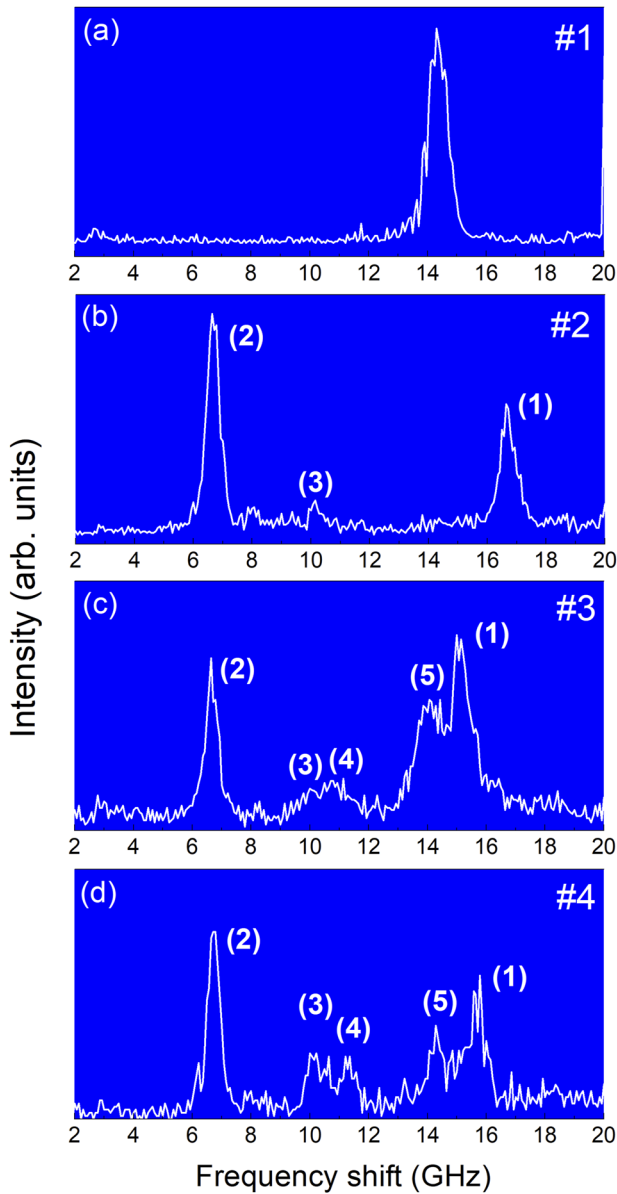
FIG. 2. Measured anti-Stokes BLS spectra at $\mu_0 H = 200$ mT for the (a) reference film (sample no. 1), (b) ASI system (sample no. 2), (c) ASI-film system with spacer 2 nm (sample no. 3), and (d) ASI-film system with spacer 10 nm (sample no. 4). BLS peaks are labeled according to the discussion in the text.

or dispersions. Details on the simulation method are given in the supplementary material.

III. DISCUSSION

A. Discussion of the dispersions

The comparison between the experimental SW dispersion measured at $\mu_0 H = 200$ mT (symbols) and the corresponding simulations
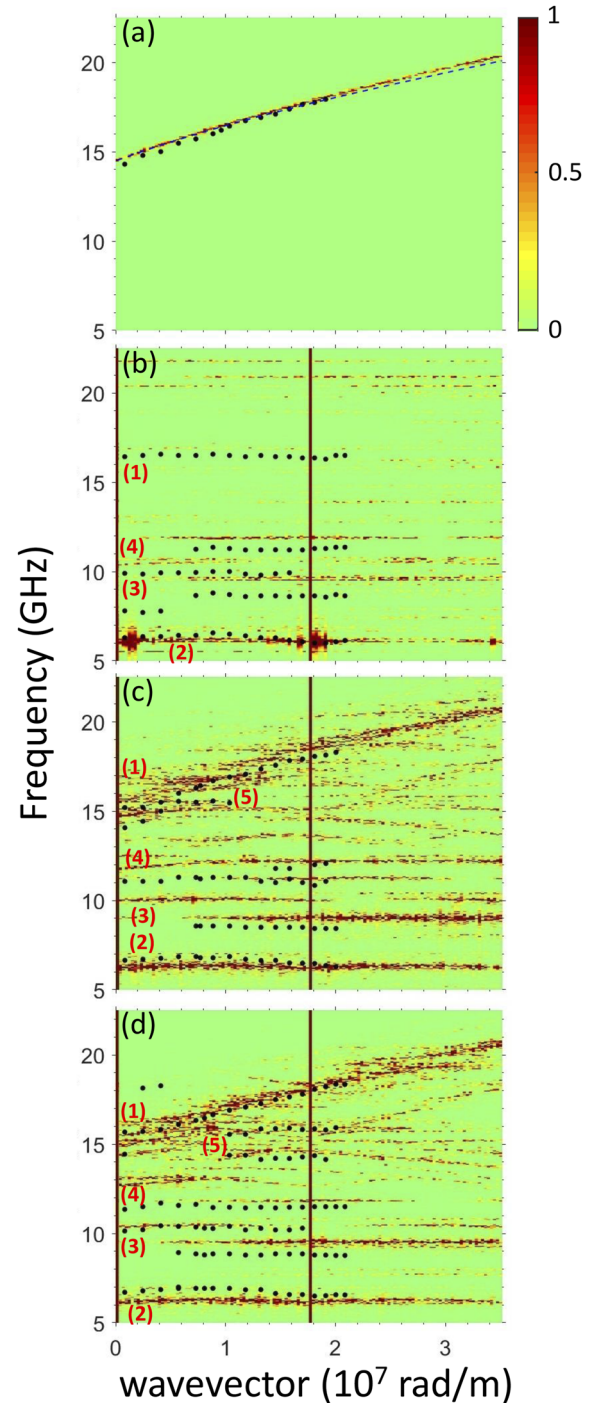
FIG. 3. Measured (symbols) and simulated (color map, indicated in the side bar on the right) dispersion curves of the (a) uncoupled reference film (sample no. 1), where the analytical dispersion is also plotted (blue dashed line) for comparison; (b) uncoupled ASI system (sample no. 2); (c) coupled ASI-film system with spacer 2 nm (sample no. 3); and (d) coupled ASI-film system with spacer 10 nm (sample no. 4). The external magnetic field is $\mu_0 H = 200$ mT. The wavevector range is extended to two BZs, and the vertical bars mark the centers $k = 0$ and $k = 2\pi/a \approx 1.8 \times 10^7$ rad/m.

for all investigated samples is shown in Fig. 3. Note that a large magnetic field was applied to avoid ambiguity and obtain magnetizations oriented in the direction of the applied field. This enables us to reveal the vertical coupling as a general mechanism beyond the specific ASI microstate.

For the uncoupled film [Fig. 3(a)], the frequency dispersion is typical for the DE mode with a monotonic frequency dependence of k.[39,40] For the uncoupled ASI, i.e., sample no. 2 [Fig. 3(b)], the measured dispersions are relatively flat (zero group velocity) except for the mode at the lowest frequency, which displays a bandwidth of about 0.5 GHz (see Fig. 1 in the supplementary material). Notably, the BLS intensity of some peaks is strongly dependent on k. This effect is reproduced in simulations [Fig. 3(b)]. For samples nos. 3 and 4 [Figs. 3(c) and 3(d)], a mode with monotonic dispersion is visible for frequencies higher than 14 GHz, partially overlapping with a flat dispersion visible in the low k-vector range at around 15 GHz [peak (5), in Fig. 3]. The measured variation of both the curves and the frequencies, compared to those of sample nos. 1 and 2, is an experimental indication of the dynamic interaction between the two layers. On the other hand, the experimental data below 14 GHz are weakly sensitive to the presence and proximity of the film underneath, which is a clear indication of the robustness of these modes with respect to the strength of ASI-film coupling. The lowest frequency mode observed in sample nos. 3 and 4 has a frequency bandwidth similar to the uncoupled ASI system (sample no. 2), suggesting that the dispersion is not affected by the presence of the film underneath.

B. Mode dynamics and ASI-film coupling

We performed micromagnetic simulations to interpret the dispersions and unveil how ASI and film modes change and hybridize in coupled systems. Hence, we can not only identify and label the peaks in the spectra but also understand the observed BLS intensity and the corresponding mode bandwidth. In fact, the dispersion

bandwidth of any mode is proportional to the dynamic stray fields it produces and, hence, proportional to the mode intensity (i.e., power).[41–43]

We interpret the SW dynamics of the ASI-film hybrid system considering the layer coupling as a "perturbation" acting on an initial set of modes, including the DE mode of the isolated film, which at 200 mT and $k = 0$ is measured at 14.3 GHz (14.5 GHz in the simulations), and the modes of the isolated (uncoupled) ASI system (Fig. 4).

The dipolar interaction between the two layers, acting as a perturbation of the ideal uncoupled layers, has two consequences. The first is the creation of a nonuniform magnetization in the film layer (which would be otherwise uniform), which causes a corresponding non-homogeneous B_{eff},[44–46] which, in turns, is responsible for the non-uniform SW mode profiles. We can address this effect as a *static coupling*. In our system, the major modification of the magnetization is found in the film layer, while the magnetization in the ASI layer is barely affected [compare Figs. 4(c) and 4(d) of Fig. 5].[47] The second effect is related to the dynamic dipolar field created by the precession of the magnetic moments in either layers, which we address as *dynamic coupling*.[42,43] In this case, at a given frequency, the phase profile of the mode in both layers is in some fixed relationship, the dynamic magnetization of each layer sharing some characteristics of the oscillation typical of the other layer (hybridization).

Using micromagnetic simulations, we find that modes of the hybrid systems with a frequency below the DE-film frequency have the same frequency and spatial profiles as the isolated ASI. Furthermore, the ASI layer of the hybrid system exhibits the same space phase profile, while their film underlayers show negligible dynamic magnetization. Thus, the two layers are dynamically uncoupled in this frequency range (compare Fig. 6 with Fig. 4). This observation is independent of the spacer layer thickness. On the other hand, the modes detected by BLS above 14 GHz are hybridized,

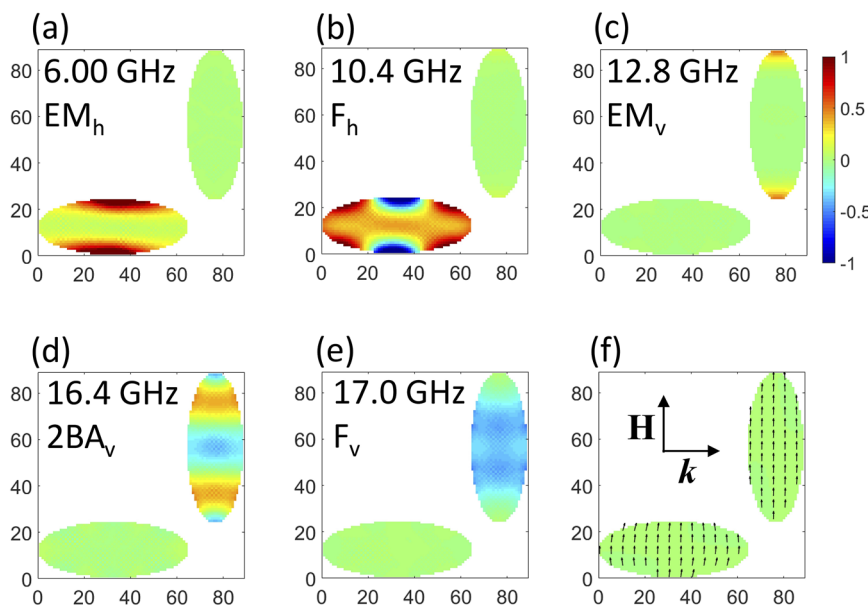**FIG. 4.** (a)–(e) Phase space profiles of the main modes in the uncoupled ASI lattice and (f) magnetization distribution, with the indication of the applied field **H** and wavevector **k** directions. Micromagnetic cell indices are shown along the x and y axes. Note that mode (e) gives rise to peak (1), mode (a) gives rise to peak (2), and mode (b) gives rise to peak (3) in the spectra of Fig. 2(b).
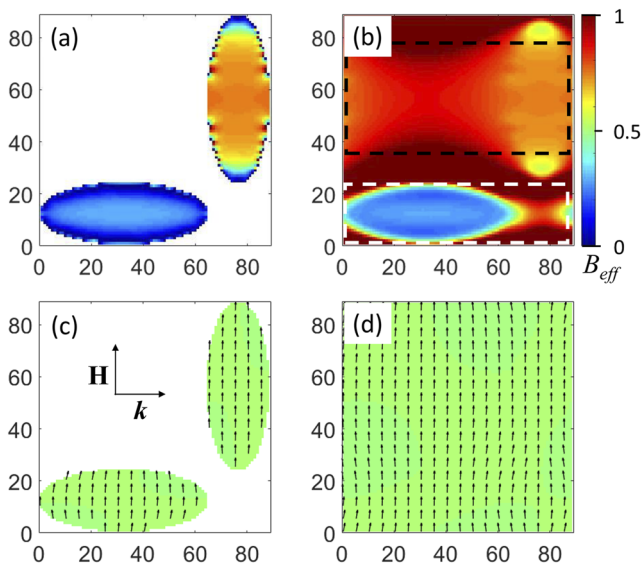
FIG. 5. Calculated effective internal field (B_{eff}) profiles (upper panels) and magnetization distribution (bottom panels) at 200 mT for sample no. 3 in [(a) and (c)] the ASI layer and [(b) and (d)] the film layer. Micromagnetic cell indices are shown along the x and y axes. In correspondence with the vertical island, in both layers, B_{eff} has similar values. Two areas of different relative minima of B_{eff} are delimited by black and white dashed rectangles, separated by a high barrier (dark red areas).

which means that at a given frequency, the two layers show similar dynamic magnetization profiles that are correlated. This effect is robust with respect to variations of the spacer layer thickness (and the applied magnetic field). We refer to this type of coupling as *dynamic coupling*. Previous works reported various types of mode hybridizations[17–19,48,49] and conversion.[50,51] However, hybridization in these cases occurred among modes relative to the same system

geometry and, hence, the same underlying magnetization. In our case, the hybridization is distinctly different from the previous reported ones: here, the hybridization occurs between modes belonging to different layers, i.e., physical structures with different geometries (film and ASI) and different underlying magnetization configurations [compare Figs. 5(c) and 5(d)].

Micromagnetic simulations reveal a variety of hybrid modes. Here, we illustrate the modes that likely have a sufficiently strong intensity to be detectable experimentally. In the following, we label ASI modes residing in the vertical islands with subscript "v" and those in the horizontal islands with subscript "h."

We describe the experimentally obtained dispersions based on our simulation results. First, the edge mode profile of the horizontal island EM_h is shown in Fig. 4(a). Although EM_h is mainly localized at the edges along the field direction, the broad area of the oscillation produces large dynamic dipolar fields responsible for the previously discussed bandwidth.[52] The corresponding edge mode of the vertical island EM_v occurs at ≈12.8 GHz, Fig. 4(c). We suspect that this mode does not lead to a detectable BLS peak since it is localized in a narrow region. The fundamental mode of the horizontal island F_h is calculated at 10.4 GHz [Fig. 4(b)] and is hybridized with an edge mode: this reduces its average intensity, appearing in the BLS spectra as peak (3) at about 10 GHz. Its calculated dispersion is rather flat, in agreement with the measured one. The fundamental mode of the vertical island F_v appears at 17.0 GHz [Fig. 6(e)], shows no nodal lines, and, hence, has a large intensity that can be associated with peak (1) of the BLS spectra measured at 16.5 GHz. Despite the large intensity, the dispersion appears flat as well. We also show the profile of an additional mode of the vertical islands at 16.4 GHz exhibiting two nodal lines perpendicular to the magnetization direction $2BA_v$ [BA stands for backward-volume character, and 2 refers to the node number, Fig. 4(d)].

When the film underlayer and ASI layer interact, we observe two main effects: (1) a change of symmetry (and, hence, amplitude) of the modes of either layer since their static magnetization changes and (2) an ASI/film hybridization of the modes, which arises if the
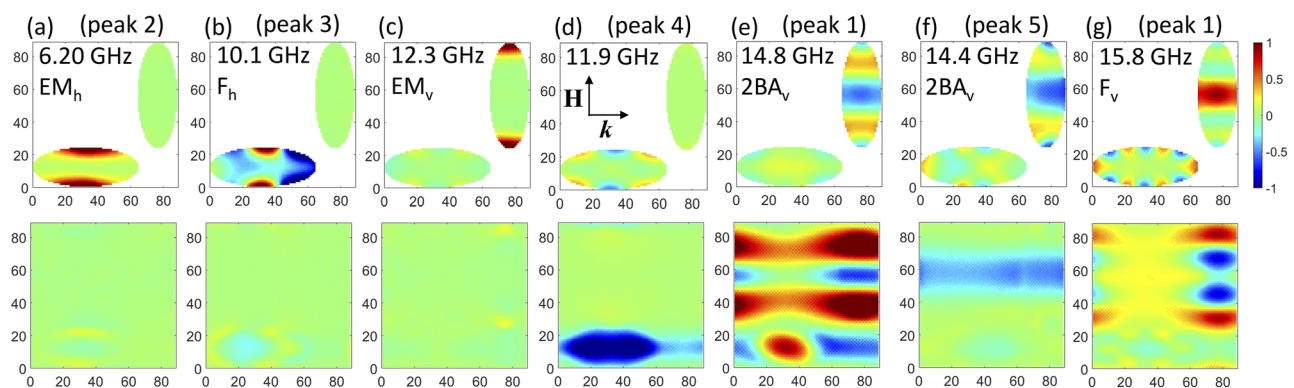

FIG. 6. Phase space profiles of the modes in the hybrid system (sample no. 3), which are also, however, illustrative of the corresponding modes in sample no. 4. Upper (lower) panels show dynamic magnetization in the ASI (film) layers. Micromagnetic cell indices are shown along the x and y axes. Modes (a)–(c) show no hybridization between the ASI and the film layer and look like those in Figs. 4(a)–4(c). Mode (d) is very intense only in the film layer, where it is reminiscent of the film DE mode. This mode is trapped in the deep minimum of B_{eff} [compare to Fig. 5(b)]. In (d), we also show the field and wavevector directions as a reference. Modes (e)–(g) are the result of the dynamic coupling between the former DE mode of the film and either the ASI mode $2BA_v$ (e) and (f) or F_v (g). The peak numbers refer to the measured spectra.

corresponding resonance frequencies are close. Two out of the four ASI-film hybridized modes [Figs. 6(d) and 6(f)] do not have any nodal lines in the film layer and, hence, can be seen as fundamental modes with a strong localization in the two different relative minima of B_{eff} [Fig. 5(b)], the deepest one occurring below the horizontal island, where the magnetization is less uniform. The other two show a phase oscillation with nodes within the primitive cell [Figs. 6(e) and 6(g)].

The first of these four modes [Fig. 6(d)] consists of a high order edge mode in the ASI layer (of negligible intensity) and an intense oscillation in the film layer, which is reminiscent of the former DE mode of the film, now strongly localized within the absolute minimum of B_{eff}, hence, at a much lower frequency. B_{eff} increases with increasing spacer, and so does the frequency of this mode: 11.9 GHz for sample no. 3 and 12.7 GHz for sample no. 4. The intensity of this mode is rather large and emerges in the spectra as "new" peak (4), absent in the uncoupled systems. Simulations show a weakly increasing dispersion at low k, which is absent in the experimental results. We observe that its mode profile in the ASI layer changes if the separation changes: this means that there is no dynamic coupling and the effect is purely coincidental.

A general rule can be derived from our simulation results: if for any given mode the dynamic coupling is present, the dynamic magnetization profile in either of the two layers is mutually hybridized, i.e., linked by a common precise dynamic quantity (wavelength, phase coherence, symmetry, etc.). This effect is robust and independent of the spacer layer and the applied magnetic field. Conversely, if the dynamic coupling is absent, the associated ASI layer and the underlayer may show different profile when an external parameter is changed.

The second fundamental mode derived from the film DE [Fig. 6(f)] consists of a $2BA_v$ mode in the ASI layer and a quasi-uniform oscillation in the film layer, which is again reminiscent of the DE of the uncoupled film, although weaker and localized in a narrow area inside the black rectangle of Fig. 5(b). Its frequency is higher than for mode (d) [14.4 GHz for both sample nos. 3 and 4, peak (5)] because the B_{eff} value it experiences is higher. This time, this mode is, indeed, the result of the dynamic coupling between ASI and film layers because of the coherence and vertical correspondence of the oscillation profiles in the layers. We verified that, different from mode (d), in this mode, the relationship between the layers is persistent independent of any parameter change.

The dynamic coupling is particularly evident for the mode of Fig. 6(e), with a perfect vertical correspondence of the in-phase precession of the two layers. The mode consists of a $2BA_v$ mode in the ASI layer, while the oscillation in the film layer resembles a backward SW with $\lambda = a/2$. This wavelength is imprinted by the ASI oscillation onto the film SW. In simulations, this mode produces an intense peak at 14.8 GHz. Hence, we associate this mode Fig. 6(e) with peak (1) in the coupled systems.

Finally, based on the simulations, we find that the mode shown in Fig. 6(g) at 15.8 GHz for sample no. 3 (15.5 GHz for sample no. 4) exhibits a F_v profile in the ASI layer and a quasi-uniform oscillation in the film layer. However, a remarkable out-of-phase precession of dynamic magnetization is found for the two layers in the vertical direction. These features are independent of the spacer and the applied field. This implies that this mode arises from the dynamic coupling. The intensity of this mode is found to be very

large. Hence, we associate this mode with peak (1) [Fig. 6(e)], leading to a broadening of the peak itself.

The three modes Figs. 6(e)–6(g) in the hybrid system are responsible for the monotonic dispersive curve starting from 14 GHz resembling the DE dispersion of the uncoupled film. With the present resolution (both experimental and computational), we cannot conclusively determine whether the structure of the dispersion at low k between 14 and 16 GHz corresponds to a crossing or an anticrossing of modes (compare to Ref. 26).

Other modes (often with incompatible profile symmetry or different node numbers) might still "occasionally" appear at the same frequency in the associated ASI and film layers. However, the reason is, in this case, pure coincidence, not interaction; hence, they are not dynamically coupled.

The dynamic coupling between layers of different geometry that was unveiled here is particularly interesting since it demonstrates the possibility of imprinting a specific wavelength, determined by the design of the ASI element and the lattice constant of the ASI to the film [$\lambda = a/2$ for mode Fig. 6(e)]. This effect is three-dimensional since the vertical coupling determines the wavelength of the in-plane propagation.

IV. CONCLUSIONS

In conclusion, we experimentally and numerically studied the spin-wave dispersion in a dipolarly coupled hybrid ASI/film system separated by a non-magnetic spacer. The experiments, supported by the micromagnetic simulations, reveal that the coupling between the layers arises in correspondence to the film mode frequency. Below that frequency, only the ASI layer is excited and exhibits mode profiles and frequencies almost identical to the uncoupled ASI lattice. Analysis of both the dispersions and the BLS spectra highlighted an appreciable bandwidth of about 0.5 GHz for the lowest frequency mode, almost insensitive to the ASI/film coupling and spacer thickness. The dispersion of the DE mode in the uncoupled film is, instead, found to be due to hybridized ASI/film modes, which showed interesting properties derived from the geometric design of the layers. Finally, we demonstrated the possibility of creating spin waves with particular wavelengths or dynamic intensity modulations in the continuous film by suitably designing the ASI geometry of the overlayer, thus, adding a new degree of freedom to control the spin-wave propagation in vertical magnonic systems.

SUPPLEMENTARY MATERIAL

See the supplementary material for details on the experimental approach, micromagnetic framework, and the experimental bandwidth estimation of the ASI mode EM_h.

AUTHOR DECLARATIONS

Conflict of Interest

The authors have no conflicts to disclose.

Author Contributions

R. Negrello: Formal analysis (equal); Investigation (equal). **F. Montoncello**: Data curation (equal); Formal analysis (equal); Investigation (equal); Resources (equal); Supervision (equal); Validation (equal); Visualization (equal); Writing – original draft (equal); Writing – review & editing (equal). **M. T. Kaffash**: Formal analysis (equal); Investigation (equal); Writing – review & editing (supporting). **M. B. Jungfleisch**: Conceptualization (lead); Formal analysis (equal); Funding acquisition (equal); Project administration (equal); Resources (equal); Supervision (equal); Writing – original draft (equal); Writing – review & editing (equal). **G. Gubbiotti**: Data curation (equal); Formal analysis (equal); Funding acquisition (equal); Investigation (equal); Project administration (equal); Resources (equal); Validation (equal); Visualization (equal); Writing – original draft (equal); Writing – review & editing (equal).

DATA AVAILABILITY

The data that support the findings of this study are available from the corresponding author upon reasonable request.

REFERENCES

[1] S. H. Skjaervo, C. H. Marrows, R. L. Stamps, and L. J. Heyderman, "Advances in artificial spin ice," Nat. Rev. Phys. **2**, 13–28 (2020).

[2] X. Zhou, G.-L. Chua, N. Singh, and A. O. Adeyeye, "Large area artificial spin ice and anti-spin ice $Ni_{80}Fe_{20}$ structures: Static and dynamic behavior," Adv. Funct. Mater. **26**, 1437–1444 (2016).

[3] E. Iacocca, S. Gliga, R. L. Stamps, and O. Heinonen, "Reconfigurable wave band structure of an artificial square ice," Phys. Rev. B **93**, 134420 (2016).

[4] S. Gliga, A. Kákay, R. Hertel, and O. G. Heinonen, "Spectral analysis of topological defects in an artificial spin-ice lattice," Phys. Rev. Lett. **110**, 117205 (2013).

[5] M. B. Jungfleisch, W. Zhang, E. Iacocca, J. Sklenar, J. Ding, W. Jiang, S. Zhang, J. E. Pearson, V. Novosad, J. B. Ketterson, O. Heinonen, and A. Hoffmann, "Dynamic response of an artificial square spin ice," Phys. Rev. B **93**, 100401 (2016).

[6] W. Bang, F. Montoncello, M. B. Jungfleisch, A. Hoffmann, L. Giovannini, and J. B. Ketterson, "Angular-dependent spin dynamics of a triad of permalloy macrospins," Phys. Rev. B **99**, 014415 (2019).

[7] V. S. Bhat and D. Grundler, "Angle-dependent magnetization dynamics with mirror-symmetric excitations in artificial quasicrystalline nanomagnet lattices," Phys. Rev. B **98**, 174408 (2018).

[8] V. S. Bhat, F. Heimbach, I. Stasinopoulos, and D. Grundler, "Magnetization dynamics of topological defects and the spin solid in a kagome artificial spin ice," Phys. Rev. B **93**, 140401 (2016).

[9] D. M. Arroo, J. C. Gartside, and W. R. Branford, "Sculpting the spin-wave response of artificial spin ice via microstate selection," Phys. Rev. B **100**, 214425 (2019).

[10] T. Dion, D. M. Arroo, K. Yamanoi, T. Kimura, J. C. Gartside, L. F. Cohen, H. Kurebayashi, and W. R. Branford, "Tunable magnetization dynamics in artificial spin ice via shape anisotropy modification," Phys. Rev. B **100**, 054433 (2019).

[11] S. Mamica, X. Zhou, A. Adeyeye, M. Krawczyk, and G. Gubbiotti, "Spin-wave dynamics in artificial anti-spin-ice systems: Experimental and theoretical investigations," Phys. Rev. B **98**, 054405 (2018).

[12] Y. Li, G. Gubbiotti, F. Casoli, F. J. T. Gonçalves, S. A. Morley, M. C. Rosamond, E. H. Linfield, C. H. Marrows, S. McVitie, and R. L. Stamps, "Brillouin light scattering study of magnetic-element normal modes in a square artificial spin ice geometry," J. Phys. D: Appl. Phys. **50**, 015003 (2016).

[13] S. Lendinez, M. T. Kaffash, and M. B. Jungfleisch, "Emergent spin dynamics enabled by lattice interactions in a bicomponent artificial spin ice," Nano Lett. **21**, 1921–1927 (2021).

[14] S. Gliga, E. Iacocca, and O. G. Heinonen, "Dynamics of reconfigurable artificial spin ice: Toward magnonic functional materials," APL Mater. **8**, 040911 (2020).

[15] M. T. Kaffash, S. Lendinez, and M. B. Jungfleisch, "Nanomagnonics with artificial spin ice," Phys. Lett. A **402**, 127364 (2021).

[16] F. Montoncello and G. Gubbiotti, "Controlling the three dimensional propagation of spin waves in continuous ferromagnetic films with an increasing out of plane undulation," Sci. Rep. **11**, 21344 (2021).

[17] S. Lendinez and M. B. Jungfleisch, "Magnetization dynamics in artificial spin ice," J. Phys.: Condens. Matter **32**, 013001 (2019).

[18] T. Dion, J. C. Gartside, A. Vanstone, K. D. Stenning, D. M. Arroo, H. Kurebayashi, and W. R. Branford, "Observation and control of collective spin-wave mode hybridization in chevron arrays and in square, staircase, and brickwork artificial spin ices," Phys. Rev. Res. **4**, 013107 (2022).

[19] J. C. Gartside, A. Vanstone, T. Dion, K. D. Stenning, D. M. Arroo, H. Kurebayashi, and W. R. Branford, "Reconfigurable magnonic mode-hybridisation and spectral control in a bicomponent artificial spin ice," Nat. Commun. **12**, 2488 (2021).

[20] S. Lendinez, M. Taghipour Kaffash, and M. B. Jungfleisch, "Observation of mode splitting in artificial spin ice: A comparative ferromagnetic resonance and Brillouin light scattering study," Appl. Phys. Lett. **118**, 162407 (2021).

[21] V. S. Bhat, S. Watanabe, K. Baumgaertl, A. Kleibert, M. A. W. Schoen, C. A. F. Vaz, and D. Grundler, "Magnon modes of microstates and microwave-induced avalanche in kagome artificial spin ice with topological defects," Phys. Rev. Lett. **125**, 117208 (2020).

[22] M. Taghipour Kaffash, W. Bang, S. Lendinez, A. Hoffmann, J. B. Ketterson, and M. B. Jungfleisch, "Control of spin dynamics in artificial honeycomb spin-ice-based nanodisks," Phys. Rev. B **101**, 174424 (2020).

[23] Y. Li, G. Gubbiotti, F. Casoli, S. A. Morley, F. J. T. Gonçalves, M. C. Rosamond, E. H. Linfield, C. H. Marrows, S. McVitie, and R. L. Stamps, "Thickness dependence of spin wave excitations in an artificial square spin ice-like geometry," J. Appl. Phys. **121**, 103903 (2017).

[24] E. Iacocca and O. Heinonen, "Topologically nontrivial magnon bands in artificial square spin ices with Dzyaloshinskii-Moriya interaction," Phys. Rev. Appl. **8**, 034015 (2017).

[25] G. Gubbiotti, A. Sadovnikov, E. Beginin, S. Nikitov, D. Wan, A. Gupta, S. Kundu, G. Talmelli, R. Carpenter, I. Asselberghs, I. P. Radu, C. Adelmann, and F. Ciubotaru, "Magnonic band structure in vertical meander-shaped $Co_{40}Fe_{40}B_{20}$ thin films," Phys. Rev. Appl. **15**, 014061 (2021).

[26] P. Graczyk, M. Krawczyk, S. Dhuey, W.-G. Yang, H. Schmidt, and G. Gubbiotti, "Magnonic band gap and mode hybridization in continuous permalloy films induced by vertical dynamic coupling with an array of permalloy ellipses," Phys. Rev. B **98**, 174420 (2018).

[27] G. Gubbiotti, *Three-Dimensional Magnonics: Layered, Micro- and Nano-structures* (Jenny Stanford Publishing, Singapore, 2019) https://www.jennystanford.com/9789814800730/three-dimensional-magnonics/.

[28] S. Gliga, G. Seniutinas, A. Weber, and C. David, "Architectural structures open new dimensions in magnetism: Magnetic buckyballs," Mater. Today **26**, 100–101 (2019).

[29]P. Fischer, D. Sanz-Hernández, R. Streubel, and A. Fernández-Pacheco, "Launching a new dimension with 3D magnetic nanostructures," APL Mater. **8**, 010701 (2020).

[30]A. May, M. Hunt, A. Van Den Berg, A. Hejazi, and S. Ladak, "Realisation of a frustrated 3D magnetic nanowire lattice," Commun. Phys. **2**, 13 (2019).

[31]S. Sahoo, A. May, A. van Den Berg, A. K. Mondal, S. Ladak, and A. Barman, "Observation of coherent spin waves in a three-dimensional artificial spin ice structure," Nano Lett. **21**, 4629–4635 (2021).

[32]S. Kempinger, Y.-S. Huang, P. Lammert, M. Vogel, A. Hoffmann, V. H. Crespi, P. Schiffer, and N. Samarth, "Field-tunable interactions and frustration in underlayer-mediated artificial spin ice," Phys. Rev. Lett. **127**, 117203 (2021).

[33]J. Li, W.-B. Xu, W.-C. Yue, Z. Yuan, T. Gao, T.-T. Wang, Z.-L. Xiao, Y.-Y. Lyu, C. Li, C. Wang, F. Ma, S. Dong, Y. Dong, H. Wang, P. Wu, W.-K. Kwok, and Y.-L. Wang, "Writable spin wave nanochannels in an artificial-spin-ice-mediated ferromagnetic thin film," Appl. Phys. Lett. **120**, 132404 (2022).

[34]E. Iacocca, S. Gliga, and O. G. Heinonen, "Tailoring spin-wave channels in a reconfigurable artificial spin ice," Phys. Rev. Appl. **13**, 044047 (2020).

[35]G. Carlotti and G. Gubbiotti, "Magnetic properties of layered nanostructures studied by means of Brillouin light scattering and the surface magneto-optical Kerr effect," J. Phys.: Condens. Matter **14**, 8199–8233 (2002).

[36]C. W. Sandweg, M. B. Jungfleisch, V. I. Vasyuchka, A. A. Serga, P. Clausen, H. Schultheiss, B. Hillebrands, A. Kreisel, and P. Kopietz, "Wide-range wavevector selectivity of magnon gases in Brillouin light scattering spectroscopy," Rev. Sci. Instrum. **81**, 073902 (2010).

[37]A. Vansteenkiste, J. Leliaert, M. Dvornik, M. Helsen, F. Garcia-Sanchez, and B. Van Waeyenberge, "The design and verification of MuMax3," AIP Adv. **4**, 107133 (2014).

[38]In simulations, we had to use the elliptical shape in order to match the experimental results: none of the many different stadium-shapes that we tried provided BLS spectra and dispersions in fair agreement with the measurements. This suggests that the "effective shape" of an island is an ellipse, although the actual shape is stadium-like, as seen in the SEM image (Fig. 1). We presume that this discrepancy between the experiment and simulations is due an effective ("active") magnetic volume that is smaller than the actual island with sharper cusps at edges due to a larger oxidation at the edges.

[39]R. W. Damon and J. R. Eshbach, "Magnetostatic modes of a ferromagnet slab," J. Phys. Chem. Solids **19**, 308–320 (1961).

[40]B. A. Kalinikos and A. N. Slavin, "Theory of dipole-exchange spin wave spectrum for ferromagnetic films with mixed exchange boundary conditions," J. Phys. C: Solid State Phys. **19**, 7013–7033 (1986).

[41]R. Zivieri, F. Montoncello, L. Giovannini, F. Nizzoli, S. Tacchi, M. Madami, G. Gubbiotti, G. Carlotti, and A. O. Adeyeye, "Effect of interdot separation on collective magnonic modes in chains of rectangular dots," IEEE Trans. Magn. **47**, 1563 (2011).

[42]J. S. Harms and R. A. Duine, "Dipolar localization of quantized spin-wave modes in thin rectangular magnetic elements," J. Magn. Magn. Mater. **557**, 169426 (2022).

[43]R. A. Gallardo, P. Alvarado-Seguel, A. Kákay, J. Lindner, and P. Landeros, "Spin-wave focusing induced by dipole-dipole interaction in synthetic antiferromagnets," Phys. Rev. B **104**, 174417 (2021).

[44]C. Bayer, S. O. Demokritov, B. Hillebrands, and A. N. Slavin, "Spin-wave wells with multiple states created in small magnetic elements," Appl. Phys. Lett. **82**, 607–609 (2003).

[45]K. Y. Guslienko, R. W. Chantrell, and A. N. Slavin, "Dipolar localization of quantized spin-wave modes in thin rectangular magnetic elements," Phys. Rev. B **68**, 024422 (2003).

[46]W. Bang, J. Sturm, R. Silvani, M. T. Kaffash, A. Hoffmann, J. B. Ketterson, F. Montoncello, and M. B. Jungfleisch, "Influence of the vertex region on spin dynamics in artificial kagome spin ice," Phys. Rev. Appl. **14**, 014079 (2020).

[47]This is due to the strong shape anisotropy of the islands.

[48]G. Gubbiotti, G. Carlotti, T. Okuno, M. Grimsditch, L. Giovannini, F. Montoncello, and F. Nizzoli, "Spin dynamics in thin nanometric elliptical permalloy dots: A Brillouin light scattering investigation as a function of dot eccentricity," Phys. Rev. B **72**, 184419 (2005).

[49]S. L. Vysotskii, S. A. Nikitov, Y. A. Filimonov, and Y. V. Khivintsev, "Hybridization of spin-wave modes in a ferromagnetic microstrip," JETP Lett. **88**, 461 (2008).

[50]F. Montoncello and L. Giovannini, "Vortex mode dynamics and bandwidth tunability in a two-dimensional array of interacting magnetic disks," Appl. Phys. Lett. **100**, 182406 (2012).

[51]S. Tacchi, B. Botters, M. Madami, J. W. Kłos, M. L. Sokolovskyy, M. Krawczyk, G. Gubbiotti, G. Carlotti, A. O. Adeyeye, S. Neusser, and D. Grundler, "Mode conversion from quantized to propagating spin waves in a rhombic antidot lattice supporting spin wave nanochannel," Phys. Rev. B **86**, 014417 (2012).

[52]F. Montoncello, S. Tacchi, L. Giovannini, M. Madami, G. Gubbiotti, G. Carlotti, E. Sirotkin, E. Ahmad, F. Y. Ogrin, and V. V. Kruglyak, "Asymmetry of spin wave dispersions in a hexagonal magnonic crystal," Appl. Phys. Lett. **102**, 202411 (2013).